Mechanisms Contributing to the Dynamic Stability of a Flexible Subscale Rocket Nozzle

Sebastian Jack [*]

German Aerospace Center (DLR), Institute of Aerodynamics and Flow Technology, Lilienthalplatz 7, Braunschweig, Germany, 38108

Michael Oschwald [†]

RWTH Aachen University, Institute of Jet Propulsion and Turbomachinery, Templergraben 55, Aachen, Germany, 52062

Thino Eggers [‡]

German Aerospace Center (DLR), Institute of Aerodynamics and Flow Technology, Lilienthalplatz 7, Braunschweig, Germany, 38108

Forced motion simulations of an overexpanded subscale rocket nozzle were performed to investigate the transient mechanisms that lead to self exciting fluid structure interaction as observed in preceded studies. The pressure response to the deformation could be separated into two regions upstream and downstream the flow separation position. Within these regions the transient part of the pressure was analyzed using fast Fourier transform based on the method of generalized aerodynamic forces. The amplitude spectrum and phase shift distribution of the pressure response could be explained by superposition of three independently acting mechanisms, the inclination-effect, the existence of a moving axial pressure wave and intrinsic oscillations caused by the turbulence created by the strong shock system. Simplified simulation setups using a bent flat plate and a detailed unsteady simulation of the flow in the undeformed nozzle were analyzed to validate these assumptions.

Nomenclature

a =   speed of sound

e =   discretization error

f =   frequency

h =   mesh cell length scale

l =   length

M =   Mach number

---

[*]Research Assistant

[†]Professor, also Coordinator Rocket Propulsion, German Aerospace Center (DLR), Institute of Space Propulsion, Lampoldshausen, Langer Grund, Germany, 74239

[‡]Head of Department

p	=	pressure
R	=	local nozzle radius normalized to throat radius r_t
r	=	local nozzle radius
S	=	running length along the nozzle wall normalized to throat radius r_t
T	=	temperature
t	=	structure thickness
v	=	velocity
X, Y, Z	=	cartesian coordinates normalized to throat radius r_t
γ	=	isentropic exponent
ε	=	expansion ratio
ϱ	=	density

Subscripts

a	=	ambient condition
BL	=	boundary layer border
e	=	exit plane
$eigen$	=	eigenvalue
FF	=	farfield
FM	=	excitation of forced motion
max	=	maximum value
min	=	minimum value
$norm$	=	normalized value
$plateau$	=	plateau value in recirculation area
pw	=	pressure wave
$S0$	=	transition from stiff to flexible structure
sep	=	flow separation position
t	=	nozzle throat
tot	=	total state
w	=	nozzle wall
∞	=	free stream state

I. Introduction

Flow separation as well as other asymmetrical effects in rocket engine nozzles can cause severe side loads that lead to deformation of the lightweight structure and, especially in presence of aeroelastic coupling effects, to damages and operation conditions critical for the engine and the surrounding structure. Multiple engine failures are documented where these phenomena were the root cause for launcher mission aborts or redesign campaigns [1–3]. The separation of the internal flow from the nozzle wall and its main characteristics were therefore investigated in many research programs. Early programs focused on experiments using scaled, simplified models [4, 5] or measurements on prototypes of the engine [6]. Data obtained during this mainly experimental phase was widely used for the design and qualification of engines as summarized by Holland [7]. A fundamentally different approach was proposed by Pekkari [8] who developed a simplified analytical model to calculate the influence of the nozzle's deformation and was able to analyze its aeroelastic stability over a wide parameter range. His model was later extended by other authors [9–12], but all versions were based on extensive simplifications. In experimental studies and numerical simulations the main characteristics of the separated supersonic flow in the undeformed nozzle were described and explained in detail during the following years [9, 10, 13–18]. Various authors have used the increasing simulation and measurement capabilities to investigate the influence of contour deformation onto the flow [19–21] and vice versa [3, 22]. Transient effects of fluid-structure interaction (FSI) were intentionally triggered in experiments [23–26], which, due to the complex flow effects, do not allow for a detailed quantitative comparison with simulation data. With increasing solver capabilities and numerical resources simulations covering the reciprocal coupling effects in supersonic nozzles became feasible, but were either described as proof of concept [27, 28] or based on simplified models for the structural domain [29–31]. Detailed analyses, using turbulent scale resolving methods such as detached eddy simulations, have been published e.g. for shock induced pressure oscillations [32] or launcher tail flow [33] but none of these cover effects caused by transient deformation of the surrounding structure.

The presented work is part of an ongoing effort to assess and evaluate the capabilities of the computational fluid dynamics (CFD) solver DLR-TAU to accurately simulate supersonic nozzle flows [34], the influence of deformation effects [35] and fluid-structure interaction [36]. In addition to the extension of the available methods for multiphysics simulations, the focus is on the quantitative evaluation of numerical errors and the systematic investigation and explanation of physical phenomena. As shown previously, experimental validation data for the transient flow phenomena in a flexible rocket nozzle are challenging to obtain and currently either not available for comparison or significantly differ in the characteristics of flow and structure. The phenomenological interpretation of the effects found by numerical simulations, presented in this work, is therefore of additional significance to identify mere numerical effects and assess their contribution to the system's characteristics and aeroelastic stability.

II. Methodology

A. CFD solver

All simulations of the flow within the computational domain have been performed using the DLR-TAU code [37–39]. It is a finite volume solver that solves the unsteady Reynolds-averaged Navier Stokes equations (RANS)

$$\frac{\partial}{\partial t} \int_V w\, dV + \oint_\Omega Fn\, d\Omega = 0 \tag{1}$$

in each finite cell volume dV of the simulation domain V. In Eq. (1) w denotes the vector of conservative variables and F that of the fluxes over the cells surface Ω with the surface normal vector n

$$w = \begin{pmatrix} \varrho \\ \varrho v \\ \varrho E \end{pmatrix} \tag{2}$$

$$F = \begin{pmatrix} \varrho v \\ \varrho v \otimes v + pI \\ \varrho E v \end{pmatrix} - \begin{pmatrix} 0 \\ \sigma \\ \sigma v + \lambda \nabla T \end{pmatrix} \tag{3}$$

where ϱ is the density, v the velocity, E the energy and T the temperature of the fluid. The stress tensor σ is calculated from the local velocity gradients and the fluid's viscosity μ.

$$\sigma = \mu \left(\nabla \otimes v + v \otimes \nabla \right) - \frac{2}{3} \mu \left(\nabla \cdot v \right) I \tag{4}$$

Because of the experimental setup [40] and the results of preceding simulations [36] the perfect gas fluid model was used for which the following equations of state apply.

$$p = \varrho RT \tag{5}$$

$$E = c_p T + \frac{1}{2} \left(v \cdot v \right) \tag{6}$$

The viscosity of the fluid was modeled by the Sutherland equation (Eq. (7)). For the heat conduction a constant Prandtl number Pr was used as shown in Eq. (8).

$$\mu = \mu_{ref} \frac{T_{ref} + C}{T + C} \left(\frac{T}{T_{ref}} \right)^{\frac{3}{2}} \tag{7}$$

$$\lambda = \frac{\mu c_p}{Pr} \tag{8}$$

$$c_p = R \frac{\gamma}{\gamma - 1} \tag{9}$$

To enable simulations of turbulent flows without resolving all time- and length-scales, the Favre averaging of the primitive variable Φ is introduced, that decomposes its instantaneous local value into an averaged part $\widetilde{\Phi}$ and a fluctuating part Φ''.

$$\Phi = \widetilde{\Phi} + \Phi'' \tag{10}$$

$$\text{with} \quad \widetilde{\Phi} = \frac{\overline{\rho \Phi}}{\overline{\rho}} \tag{11}$$

$$\overline{\Phi}(x, t) = \lim_{N \to \infty} \frac{1}{N} \sum_{i=1}^{N} \Phi_i(x, t) \tag{12}$$

Introducing the described averaging into the system of conservation equations, the flux density vector is extended by the turbulent part F_t.

$$F_t = \begin{pmatrix} 0 \\ \sigma_t \\ \widetilde{v} \sigma_t - c_p \frac{\mu_t}{Pr_t} \nabla \widetilde{T} \end{pmatrix} \tag{13}$$

$$\text{with} \quad \overline{\rho} \sigma_t = \overline{\rho v'' \otimes v''} \tag{14}$$

$$\overline{\rho} \widetilde{k} = \frac{1}{2} \overline{\rho (v'' \cdot v'')} \tag{15}$$

$$\mu_t = \overline{\rho} \frac{\widetilde{k}}{\omega} \tag{16}$$

A constant turbulent Prandtl number Pr_t was used in all simulations. For the turbulent Reynolds stresses σ_t the transport equation Eq. (17) based on the findings by Rotta [41], derived by Launder et.al. [42] and extended for the diffusion terms by Daly and Harlow [43] is being used [*].

---

[*]For better readability the transport equations are written in index notation using the Einstein summation convention and the Kronnecker-delta δ_{ij}.

$$\frac{\partial \overline{\rho v_i'' v_j''}}{\partial t} + \frac{\partial \overline{\rho \widetilde{v}_k v_i'' v_j''}}{\partial x_k} = \tag{17a}$$

$$- K_P \overline{\rho} \left(\overline{v_j'' v_k''} \frac{\partial \widetilde{v}_i}{\partial x_k} + \overline{v_i'' v_k''} \frac{\partial \widetilde{v}_j}{\partial x_k} \right) \tag{17b}$$

$$- 2\overline{\rho} \frac{\widetilde{k}}{\omega} \overline{\frac{\partial v_i''}{\partial x_k} \frac{\partial v_j''}{\partial x_k}} \tag{17c}$$

$$+ K_P \overline{p'' \left(\frac{\partial v_i''}{\partial x_j} + \frac{\partial v_j''}{\partial x_i} \right)} \tag{17d}$$

$$- K_\Pi \frac{\partial}{\partial x_k} \left[\overline{\rho v_i'' v_j'' v_k''} \right. \tag{17e}$$

$$- \frac{\widetilde{k}}{\omega} \frac{\partial \overline{\rho v_i'' v_j''}}{\partial x_k} \tag{17f}$$

$$+ \left. \overline{p'' \left(\delta_{ik} v_i'' + \delta_{ik} v_j'' \right)} \right] \tag{17g}$$

The production term Eq. (17b) can be calculated directly from the velocity gradients. With the assumption of local isotropic turbulent length scales the dissipation term Eq. (17c) can be calculated using the dissipation rate ω as given in Eq. (18) [41]. As proposed by Chou [44] the pressure strain correlation in Eq. (17d) and Eq. (17g) is modeled using the Poisson equation Eq. (19). The turbulent velocity fluctuations in Eq. (17e) are modeled using the generalized gradient diffusion hypothesis Eq. (20) by Daly and Harlow [43].

$$2\overline{\rho} \frac{\widetilde{k}}{\omega} \overline{\frac{\partial v_i''}{\partial x_k} \frac{\partial v_j''}{\partial x_k}} = \frac{2}{3} \delta_{ij} \omega \tag{18}$$

$$\overline{p'' \left(\frac{\partial v_i''}{\partial x_j} + \frac{\partial v_j''}{\partial x_i} \right)} = -\overline{\rho} \frac{\omega}{\widetilde{k}} \left(\overline{v_i'' v_j''} - \frac{2}{3} \delta_{ij} \widetilde{k} \right) \tag{19}$$

$$\overline{\rho v_i'' v_j'' v_k''} = -\frac{\overline{\rho} \widetilde{k}}{4\omega} \overline{v_k'' v_l''} \frac{\partial \overline{v_i'' v_j''}}{\partial x_l} \tag{20}$$

The characteristic turbulent scale ω is modeled using the baseline ω-equation by Menter [45].

$$\frac{\partial \overline{\rho} \omega}{\partial t} + \frac{\partial \overline{\rho} \widetilde{v}_k \omega}{\partial x_k} =$$

$$K_\omega \gamma_\omega \sigma_{t,ij} \frac{\omega}{\widetilde{k}} \frac{\partial \widetilde{v}_i}{\partial x_j} - \beta_\omega \overline{\rho} \omega^2$$

$$+ \frac{\partial}{\partial x_j} \left[(\mu + \sigma_\omega \mu_t) \frac{\partial \omega}{\partial x_j} \right] + CD_\omega \tag{21}$$

The constants γ_ω, β_ω, σ_ω and the cross diffusion term CD_ω are implemented as published by Menter in [45] (A2-A10). In the presence of strong shocks the original formulation of the turbulence model tends to drastically overestimate the production of turbulent stresses. Correction factors, calculated from the Mach number M and turbulent Mach number M_t upstream the shock, are therefore used for the turbulent quantities as described in detail by Karl et. al. in [46]. The calculation of these factors require a shock sensor, which is implemented in DLR-TAU evaluating the local pressure gradient.

$$K_P = 1 - \max \left[0; 0.63 \left(2 - \exp\left(1.2\widetilde{M} \right) - \exp\left(0.02\widetilde{M} \right) \right) \right] \tag{22}$$

$$K_\Pi = K_P; \quad K_\omega = K_P^{\frac{1}{6}} \tag{23}$$

$$\text{with} \quad \widetilde{M} = 1 - (M - M_t) \tag{24}$$

For the flux vector splitting in space an upwind scheme and gradient reconstruction, to achieve second order accuracy, were used. The second order accurate dual-time-stepping scheme by Jameson [47] was applied for time integration.

B. CSM solver and interpolation

To obtain the shape of the deformed nozzle structure, the modal analysis solver of the commercial software MSC Nastran was used.

The software uses the total Lagrange formulation of the kinematic relations of the solid body in its reference state x_0. Together with the derived displacement tensor D and the derived deformation gradient, the Green-Lagrange strain tensor ϵ and the stress tensor σ are being formulated based on Hooke's law and linear elastic material properties, where λ and μ are the Lamé coefficients calculated from the Young's modulus E and the Poisson's ratio ν.

$$F = \frac{\partial x}{\partial x_0} = \nabla_0 D + I \tag{25}$$

$$\epsilon = \frac{1}{2} \left(F^T F - I \right) \tag{26}$$

$$\sigma = \text{tr}(\epsilon)\lambda I + 2\mu\epsilon \tag{27}$$

$$\text{with} \quad \lambda = \frac{\nu E}{(1 + \nu)(1 - 2\nu)} \tag{28}$$

$$\mu = \frac{E}{2(1 + \nu)} \tag{29}$$

For an arbitrary but valid variation of the displacement tensor δD the conservation law for the control volume V with the border Ω is

$$\int_V \varrho \frac{\partial^2 D}{\partial t^2} \delta D dV + \int_V \frac{\sigma}{\delta \epsilon} dV = \int_V b \delta D dV + \int_\Omega s \delta D d\Omega \tag{30}$$

where b denotes the internal volume specific forces of the system and s the Neumann boundary condition applied as stresses to its border Ω.

By the method of finite elements and according shape functions for each control volume the conservation law can be reduced to the following discrete formulation of an initial boundary value problem containing only the system's mass matrix M, the displacement tensor D, the material damping d and the internal (*int*) and external (*ext*) forces f.

$$M \frac{\partial^2 D}{\partial t^2} + d \frac{\partial D}{\partial t} + f_{int}(D) = f_{ext} \tag{31}$$

By neglecting structural damping and external forces the structure's eigen shapes and corresponding frequencies can directly be derived from Eq. (31) by calculating its eigenvectors and eigenvalues. For the temporal discretization of Eq. (31) the integration scheme proposed by Newmark [48] was used to reduce the dimensions of the system which was then solved by application of the generalized-α method proposed by Chung and Hulbert [49].

The resulting local distribution of the displacement data was interpolated to the CFD mesh using radial basis functions. A detailed description of the used interpolation method, including its numerical validation, has been published by Spiering et. al. [50]. To ensure a conservative wall thickness of the thin nozzle structure, the displacement vector of the outer wall boundary was reconstructed based on the interpolation results on the inner wall and the local deformed coordinate gradients for each node on the outer wall boundary of the CFD mesh.

III. Test case

Figure 1 shows a radial cross section of the rotational symmetric simulation domains. The geometry used for this investigation is a truncated ideal contour (TIC) nozzle with a throat radius of $r_t = 10\,\text{mm}$, an expansion ratio of $\varepsilon = 18.47$ and a maximum Mach number of $M = 5.3$ using cold nitrogen ($T_{tot} = 300\,\text{K}$) as working fluid. It is designed to be full flowing for a nozzle pressure ratio of $NPR = p_{tot}/p_a = 50$.

Table 1   Fluid properties

isentropic exponent	γ	1.4	
specific gas constant	R	296.8	$\text{J}\,\text{kg}^{-1}\,\text{K}^{-1}$
reference viscosity	μ_{ref}	1.663×10^{-5}	Pa s
reference temperature	T_{ref}	273	K
Sutherland constant	C	107	K
Prandtl number	Pr	0.72	
turbulent Prandtl number	Pr_t	0.9	
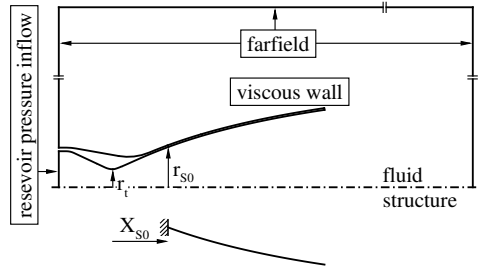
Fig. 1   Sketch of the numerical simulation domains and boundary conditions

The CFD domain used for all nozzle simulations described in the following sections is shown above the dashed symmetry line in Fig. 1. It has been cropped for better visibility, because the original size of the surrounding farfield is extended to a radius of $r_{FF} = 50\,r_t$ and a downstream length of $l_{FF} = 100\,r_t$. At the nozzle inlet the total state of the fluid is prescribed by the boundary condition (here $T_{tot} = 300\,\text{K}$ and $p_{tot} = 3.0\,\text{MPa}$). The velocity is set to be perpendicular to the cell faces and its magnitude is calculated assuming an ideal isentropic expansion to the adjacent cells' static conditions (reservoir-pressure inflow). All walls have been modeled using adiabatic viscous wall boundary conditions, thus applying a no-slip condition that sets the local fluid velocity to that of the, possibly moving, wall (zero in all cases of no transient deformation) and the wall-normal heat flux to zero. All simulations of the flow within the nozzle were performed on a hybrid mesh of the full 360° three-dimensional geometry to avoid symmetric effects forced by internal boundary conditions. The mesh used for all simulations contains approximately 9.5 million nodes.

In the part below the dashed symmetry line Fig. 1 shows a sketch of the structural domain. The structure of the nozzle is represented by a rotational symmetric thin geometry (solid line) that is clamped, i.e. fixed in all six degrees of freedom, at X_{S0}. Downstream the clamping position the model is free to move and loaded by the forces caused by the surrounding fluid. For all simulations the flexible part of the structure was represented by a mesh consisting of thin quadrilateral shell elements as described by MacNeal [51]. The mesh consists of 17 820 shell elements and was originally designed to simulate fluid structure interaction in the nozzle. Upstream the interface point at an expansion ratio of $\varepsilon_{S0} = 5$, i.e. $R_{S0} = \sqrt{5}$ at $X_{S0} = 3.08$, the walls are considered ideal stiff because in realistic engine configurations this region is usually manufactured out of solid metal to house the required cooling system. To scale its structural behavior and ensure the material parameters lie within a realistic range to manufacture, a quasi-isotropic glass-fiber reinforced plastic laminate with a fiber volume ratio of 43 % is used as material for the nozzle's structure. It has an elastic modulus of $E = 2 \times 10^{10}\,\text{Pa}$, a Poisson's ratio of $\nu = 0.18$ and a density of $\varrho = 2100\,\text{kg/m}^3$ [52]. For more information on the scalability considerations of the structural model see [36].

IV. Discretization error

A. CFD domain

The influence of the spatial resolution of the fluid domain onto the relevant flow quantities has been evaluated using the method proposed by Roache [53]. A coarse and fine mesh have been created by scaling all cells edge lengths with a factor of $h_{rel} = 1.5$ and $h_{rel} = 1/1.5$ (table 2).

Table 2   Mesh properties

mesh	index	h_{rel}	number of nodes
coarse	1	1.5	3.1×10^6
reference	2	1.0	9.5×10^6
fine	3	1/1.5	31.0×10^6

From the results calculated on all three meshes the separation position x_{sep} and the average pressure downstream the separation line $p_{plateau}$ have been extracted to calculate the error as shown in Eq. (32).

$$e_{12} = \left| \frac{q_2 - q_1}{1 - h_{rel}^p} \right| \tag{32}$$

Herein q is the chosen integral flow characterizing quantity (x_{sep} or $p_{plateau}$), $h_{rel} = 1.5$ the constant refinement factor and the indices 1, 2 and 3 mark the coarse, medium and fine mesh. Along discontinuities the CFD solver reduces the order of spatial gradient calculation to one, to ensure numerical stability, $p = 1.75$ has therefore been used for the order of convergence as proposed for the DLR-TAU code and evaluated by Rakowitz [54]. For better evaluation relative errors have been calculated by means of characteristic scales. Because the absolute extrapolated value of the separation position depends on the choice of the coordinate system's origin and is therefore not suited for normalization, the nozzle's divergent length has been used as characteristic length scale for calculation of the relative errors. The relative error of the plateau pressure has been calculated with regard to the extrapolated estimate of the exact solution.

Figure 2 shows the discretization error calculated for the separation position. For the chosen mesh ($h_{rel} = 1$) and all pressure ratios it has a maximum value of 10.97 mm, or 9.33 % of the divergent nozzle length. It should be noted that, for NPR = 40 and the coarse mesh, the separation line lies close to the nozzle exit and the recirculation of the outer fluid suppresses further downstream movement. This results in an underestimation of the error.

The discretization error calculated for the plateau pressure is shown in Fig. 3. For the chosen mesh ($h_{rel} = 1$) and all pressure ratios it has a maximum value of 8571 Pa, or 9.1 % and decreases significantly with decreasing NPR. For large pressure ratios and coarse meshes the plateau region becomes smaller, as described earlier, resulting in steeper pressure gradients and thus larger values of the errors.

All following simulations use a pressure ratio of NPR = 30 for which the error estimation yields 7.7 % using the
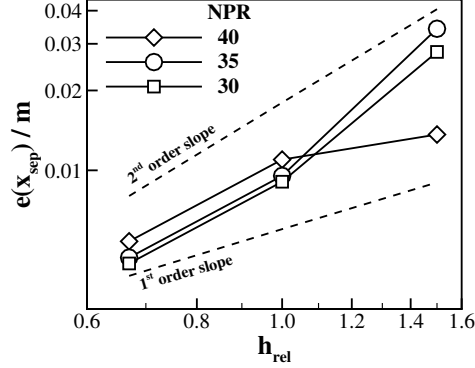
Fig. 2 Error in separation position x_{sep} over mesh refinement scale h_{rel}
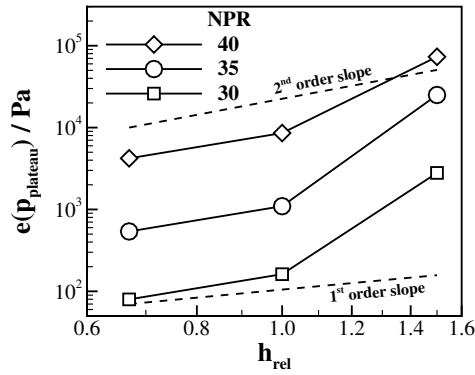
Fig. 3 Error in plateau pressure $p_{plateau}$ over mesh refinement scale h_{rel}

separation position and 0.2 % using the plateau pressure.

B. CSM domain

For assessment of the spatial discretization error of the structural domain, a fine mesh has been created by scaling all mesh cells' length scales with a factor of $h_{rel} = 1/4$. Eq. (32) was used to calculate the discretization error with the eigen frequency of the first four eigenmodes as characteristic quantity q and an order of convergence of $p = 1$ due to the linear shape function of the used elements. The error has a maximum value of 2.89×10^{-2} Hz, or 1.58×10^{-3} % at the fourth eigenmode. The maximum difference in the local displacement vector norm calculated on the used relative to the fine mesh is 0.133 %.

V. Forced motion nozzle simulations

As a first step to analyze the transient flow and its effects onto the dynamic stability of the coupled system, forced oscillation simulations of the nozzle have been carried out. This methodology has been developed and used widely in application to panel and wing flutter stability analysis (see. e.g. the work by Dowell or Muhlstein [55, 56] or more recent applications to panels in transsonic flow by Lübker et. al. [57] and especially the detailed numerical work by

11

Alder [58]). Preceding two-way coupled simulations of the fluid-structure interaction in the nozzle have shown that, in case of unstable system parameters, the nozzle structure tends to oscillate in the shape of the eigenmode with the lowest eigenfrequency. Higher structural frequency oscillations are either not excited or damped throughout the simulation time. The main coupling process that determines energy transfer from the fluid to the structure, and vice versa, is therefore closely related to the so called *single-mode flutter*.

A. Mean flow field

Figure 4 shows the results of the CFD simulation in a radial cross section through the nozzle simulation domain. Because the nozzle was designed to be full flowing at an inlet pressure of $p_{tot} = 5.0$ MPa the fluid expands to supersonic velocities and, due to the overexpansion, separates from the nozzle wall at $X_{sep} = 8.1$. Close to the flexible nozzle wall, the flow field can therefore be divided into two generally different regions. Upstream the separation position (marked with $\boxed{1}$ in Fig. 4) the flow outside the boundary layer is supersonic and further expanded in downstream direction. An inclined shock forms at the separation line, which can be identified by the high density gradient shown in the lower half of the contour plot of Fig. 4). Downstream this separation shock, the fluid surrounding it is sucked into the nozzle forming a recirculation region (marked with $\boxed{2}$ in Fig. 4 and recognizable by the stream traces in its lower half). A strong vertical shock (the Mach disk) forms in the nozzle's center.

The aforementioned effects cause the wall pressure to decrease continuously in the attached region ($\boxed{1}$ in Fig. 4) to a value of $p_{sep} = 0.24\ p_a$ at the separation position. A steep gradient is then induced by the separation shock. Further downstream the pressure reaches a value of $p \approx 0.9\ p_a$ in the recirculation region ($\boxed{2}$ in Fig. 4). These flow patterns match the descriptions of separated nozzle flows [9, 10, 59] and have been validated by comparison to experimental data [34, 35, 40].
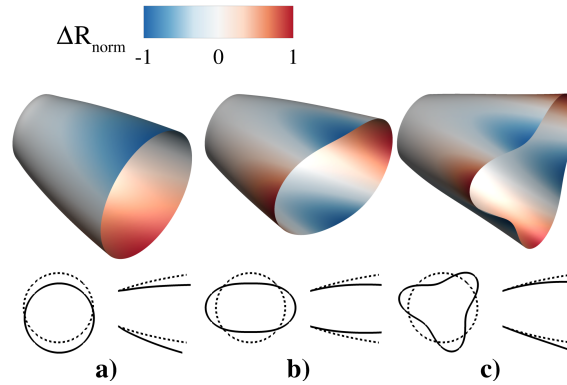
B. Shape and frequency of the eigenmodes

For the forced motion analysis the nozzle's eigenmodes with the lowest eigenfrequency were used. Figure 5 shows the shape of the first three eigenmodes (isometric view and solid lines) together with the shape of the undeformed nozzle (dashed lines). In the upper part it shows an isometric view of the respective mode, colored by the local radial displacement normalized to its global maximum value ($\Delta R_{norm} = \Delta R / \Delta R_{max}$). Because the modal analysis of the structure returns the mode shapes as eigenvectors of the mechanical systems and their frequencies as its eigenvalues, the absolute value of the returned displacement vectors have no physical representation. The displacements in Fig. 5 were therefore scaled to have a maximum of 30 % of the nozzle's exit radius R_e for good visibility.

The three modes with the lowest eigenfrequencies f_{eigen} are the bending (Fig. 5a), oval (Fig. 5b) and triangular (Fig. 5c) shaped ones. Because a bent nozzle shape has not been observed in the previously performed coupled simulations it was excluded from the presented investigation. Figure 6 shows the eigenfrequency of the mentioned eigenmodes
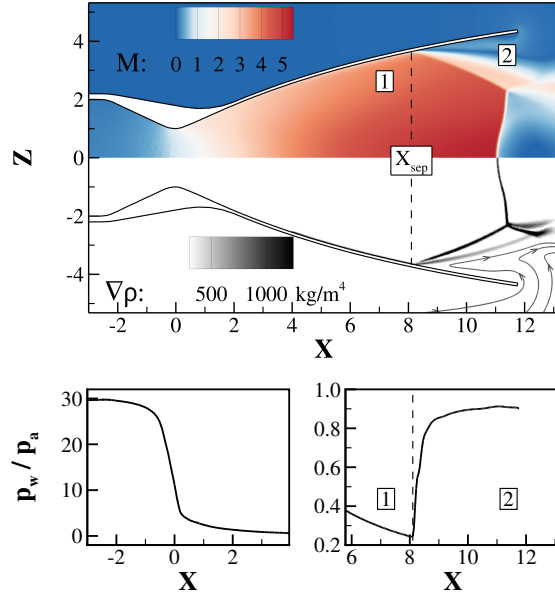
Fig. 4 **Distribution of Mach number M, density gradient $\nabla\varrho$ and wall pressure p_w normalized by ambient pressure p_a in radial cross section**

Fig. 5 **Shape of the eigenmodes (solid lines) and the undeformed nozzle (dashed lines)**

as a function of the wall thickness t_w of the structure. As expected, each mode's eigenfrequency rises with the wall thickness. Because of the different gradient of this increase, the mode with the lowest eigenfrequency changes from the triangular to the oval one in the vicinity of $t_w = 0.95$ mm. None of the eigenmodes can therefore be rated the one with the smallest eigenfrequency in the relevant wall thickness range, because this value is close to the stability border of the coupled system. The oval and triangular shaped modes were thus both investigated in the forced motion analysis. For the simulations the frequency has been varied in a range from $f_{min} = 1$ Hz, to cover the regime with low influence of inertia effects, to $f_{max} = 1$ kHz which is sufficiently larger than the eigenfrequencies and those of the main displacement patterns observed in the coupled simulation. The frequency of $f_{FSI} = 526$ Hz was of particular interest, because it was the dominant one in the coupled system.

13
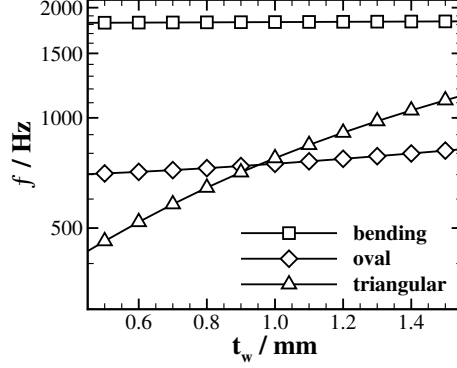
Fig. 6 Influence of the wall thickness on the eigenfrequency of the nozzle's eigenmodes

C. Dynamic excitation and post-processing

During the simulations the earlier described eigenmodes have been applied to the nozzle structure in a sinusoidal distribution over time with a maximum radial displacement of $\Delta R_{max} = 1\% R_e$ to ensure the flow response to the excitation can be measured and is also well within the linear region. The time step has been set to a maximum of $\Delta t_{max} = (100\ f_{FM})^{-1}$ to resolve the dynamic flow features and lowered when necessary for numerical stability. To ensure initial effects are propagated through the flow field, the first five periods have been ignored in the data analysis. Following this initialization, at least five, for the excitation frequencies larger than 100 Hz ten, excitation periods have been simulated and processed to also capture effects with frequencies significantly lower than the excitation itself.

D. Pressure response

The forced oscillation of the nozzle's shape leads to a dynamic pressure response at its wall. Figure 7 shows the spectrum of the wall pressure amplitude $\hat{p}_w$ at three axial positions in the attached region (black, $X = 6$) close to the separation line (red, $X = 8$) and in the recirculation region (blue, $X = 9$). The shown data have been obtained from the results of a forced motion simulation of the oval mode shape excited with $f_{FM} = 100$ Hz by a fast Fourier transform. In the attached region ($X = 6$ and $X = 8$) the pressure response amplitude spectrum shows distinct peaks at the excitation frequency (normalized frequency of $f_{norm} = f/f_{FM} = 1$, marked with a dashed vertical line) and each of its whole number multiple. For the excitation frequency the amplitude is about two orders of magnitude larger than those of the higher harmonic contributions. This spectrum is what one would expect to observe for a flow that is forced to follow the oscillating wall shape.

Within the recirculation region ($X = 9$) the pressure amplitude shows no notable peak but a broad distribution. At low frequencies ($f < 200$ Hz) the amplitude has a nearly constant value of $\hat{p}_w \approx 350$ Pa. The amplitude then decreases with increasing frequency prior to the second plateau beginning at approximately $f = 1$ kHz with values $\hat{p}_w < 1$ Pa. In this region the flow's behavior seems to be independent from the external excitation but caused by an intrinsic

14

mechanism.
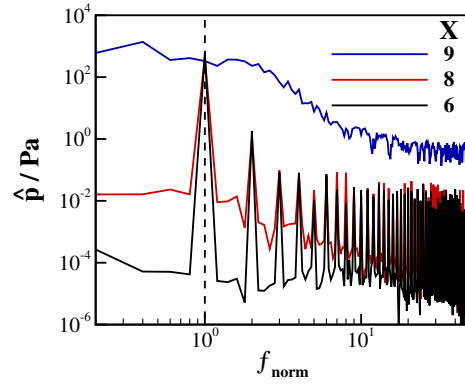
Fig. 7 **Pressure amplitude** $\hat{p}$ **spectrum for oval mode excited with** f_{FM} = 100 Hz **at circumferential position of maximum radial displacement**

The concept of generalized aerodynamic forces is being used to assess the influence of the dynamic pressure response to the overall system stability which is the main focus of this work. By application of a Laplace transform, the pressure response signal can be divided into its real and imaginary part. Theoretical investigations show that the imaginary part $\Im(p_w) = \hat{p}_w \sin \Delta\Phi_p$ is a measure of the dynamic stability contribution (for detailed information and derivation see chapter 3.5 of [60] or [58]). Aside from the aforementioned pressure amplitude $\hat{p}_w$ the phase shift between the external excitation mechanism (here: displacement of the nozzle wall) and the pressure response $\Delta\Phi_p$ is of notable concern.
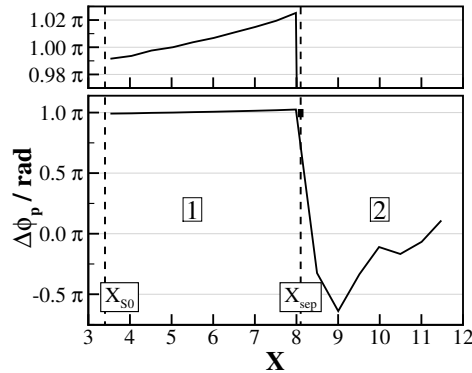
Fig. 8 **Pressure phase shift** $\Delta\Phi_p$ **over axial position for oval mode excited with** f_{FM} = 100 Hz **at circumferential position of maximum radial displacement**

Figure 8 shows this phase shift for the excitation frequency (f_{norm} = 1) at the circumferential position of the maximum radial displacement. Because the pressure response in the recirculation region (2) is unrelated to the excitation, the phase shift distribution there is of little informative value. In the attached region (1), the phase shift shown in detail in the upper part of Fig. 8 is close to π which is what one would expect for the pressure distribution within a supersonic nozzle. A change in the local nozzle wall radius causes a counter-acting change in the local wall pressure due to the changed wall inclination (see [61] for a more detailed description). In the following this mechanism

will therefore be referred to as the inclination-effect. The axial gradient of the phase in this region is non-zero but almost constant and is imposing the inclination-effect. This indicates the existence of a superposing axial wave that is being generated at the clamping point of the structure (X_{S0}) and moves downstream. All of the phenomena described so far can be observed in the data obtained from the forced motion simulations applying the oval (ova) and triangular (tri) shaped eigenmodes for the whole frequency range.

To examine the influence of the pressure phase shift in more detail, the function shown in Eq. (33) was fitted to the data in the attached region.

$$\Delta\Phi_p = \frac{\partial\Delta\Phi_p}{\partial X} \ (X - X_{S0}) + \Delta\Phi_{p0} \tag{33}$$

Figure 9 shows the function's coefficients obtained by this fit over the excitation frequency (symbols) and a linear regression line for each mode shape and coefficient (solid and dashed lines).
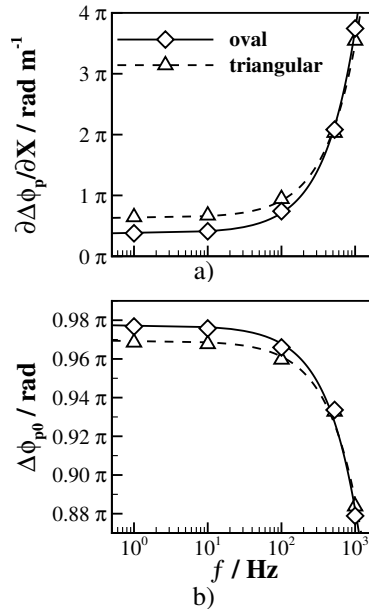
Fig. 9   a) gradient ($\partial\Delta\Phi_p/\partial X$) and b) intercept ($\Delta\Phi_{p0}$) of linear fit to pressure phase shift

The intercept of the pressure phase, $\Delta\Phi_{p0}$ shown in Fig. 9b, tends to π for low excitation frequencies as expected by explanation of the inclination-effect earlier. With rising excitation frequency the value decreases nearly linearly. This linear frequency dependent effect indicates the existence of an inertia effect.

The axial gradient of the phase shift, $\partial\Delta\Phi_p/\partial X$ shown in Fig. 9a, tends to zero for low excitation frequencies, has a positive frequency gradient and also follows the linear regression line quite well. This behavior matches the assumption of the existence of a downstream moving pressure wave. When the flexible nozzle extension deforms, the wall-normal part of the deformation causes a change of the wall's curvature in the vicinity of the clamping position *S0*, which leads

16

to a local deflection of the flow and thus, due to the supersonic velocity, either an additional expansion or compression, depending on the curvature change's sign. For the applied harmonic oscillation of the oval and triangular eigenmode this mechanism leads to an oscillating pressure disturbance located in the boundary layer that acts as a source for the axially moving pressure wave. Assuming an ideal gas, the velocity at which the wave, moves downstream (v_{pw}) can be calculated from the convective (v_∞) and the sonic velocity (a) as shown in Eq. (34).

$$v_{pw} = \frac{2\pi}{\frac{\partial \Delta \Phi_P}{\partial X}} f \tag{34}$$

$$= v_\infty + a \tag{35}$$

$$= v_\infty + \sqrt{\gamma R T} \tag{36}$$

Because of the strong expansion of the flow inside the nozzle, the temperature T as well as the farfield velocity v_∞ (here: the velocity at the boundary layer border) depend on the axial position. The wave propagation velocity v_{pw} is therefore also position dependent. Figure 10a shows the fluid's velocity extracted from the steady state initial solution at a constant wall distance of $d_w = 1$ mm. Together with the local fluid temperature along the same line, the wave propagation velocity in the boundary layer vicinity can be calculated (v_{pw} shown in Fig. 10c). In the region of interest, between the pressure disturbance source located at X_{S0} and the end of the attached region at X_{sep}, the wave propagation velocity shows a slight increase which can explain the rising gradient of the phase shift shown in Fig. 8.
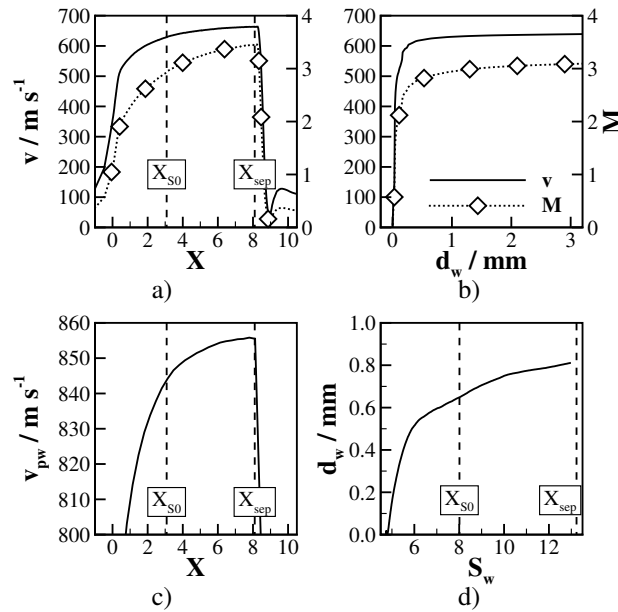
Fig. 10   Velocity profiles and boundary layer thickness for mean flow field in the nozzle

This estimate of the local wave propagation velocity is based on the assumption that the fluid's state at a wall distance of $d_w = 1$ mm is defining its boundary layer properties. To support this assumption the velocity profile at X_{S0} normal to the nozzle wall is shown in Fig. 10b. At a wall distance of $d_w = 1$ mm the fluid has indeed reached a velocity plateau, but the chosen distance also seems close enough to the highly accelerated part of the boundary layer. Figure 10d shows the boundary layer thickness over the running length along the nozzle's inner wall normalized to the throat radius (S_w). It has been obtained from the flow field by application of the widely-used criterion of $v_{BL} = 0.99\, v_\infty$ with $v_\infty = v\,(d_w = 1\,\text{mm})$. According to this data the boundary layer thickness lies close to but within the selected wall distance of $d_w = 1$ mm within the complete attached region.

Based on the findings described so far the following assumptions for explanation of the observed effects are made. The pressure response to the deformation excitation in the attached region is dominated by the inclination-effect (assumption *A1*). A superposing axially moving wave is generated at the position of the flexible nozzle manifold and moves downstream near the wall (assumption *A2*). The pressure response in the recirculation region is independent of the excitation and intrinsic to the flow structure within the highly overexpanded nozzle (assumption *A3*).

Assumption *A1* has been explained earlier and also fits the behavior of flat plates and wings being displaced by aerodynamic loads in supersonic flow regimes. To verify *A2* and *A3* simplified simulation setups have been created to allow for a more detailed investigation. These will be described in the following sections.

VI. Bent flat plate

To support assumption *A2* made in section V.D simulations of the flow over a bent flat plate have been carried out. The aim of these simulations was to check whether the axially propagating pressure wave can also be observed in simplified simulations of higher resolution using a similar numerical setup. Quantitative data for the properties of the wave can be obtained and compared with those of the nozzle simulations, due to the simplification, especially the constant free stream conditions.

A. Simulation setup

Figure 11 shows a sketch of the two-dimensional computational domain used for all simulations described in this section. The sketch is to scale in axial direction but has been cut in wall normal direction for better visibility. From the left the flow enters with the free stream condition equivalent to that at $d_w = 1$ mm and X_{S0} within the nozzle simulations.

The applied farfield boundary condition is also given in table 3. Upstream the viscous walls an inviscid wall was placed to avoid numerical instabilities due to the contact of the farfield and viscous wall boundary condition. To achieve a boundary layer thickness similar to that observed in the nozzle simulations the length of the viscous wall boundary upstream the plate's joint was adapted accordingly. During the simulations a deflection angle $\theta = \hat{\theta}\,\sin\left(2\pi t\, f_{FM}\right)$ has been applied to the downstream part of the plate using the same interpolation and deformation methods as in the nozzle
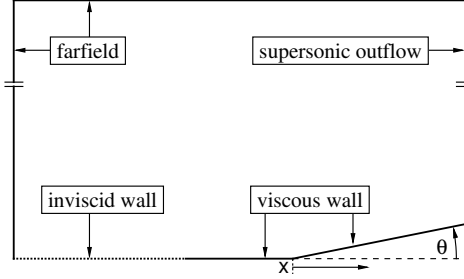
Fig. 11 Sketch of the numerical simulation domains and boundary conditions for the flat plate simulations

simulations. A preliminary study using different deflection amplitudes ($\hat{\theta} = 0.5°, 1°, 5°$) has shown that the chosen value of one degree causes measurable effects in the system's pressure response which are well below the level of non-linearity. All simulations have been carried out using a physical time step size of $\Delta t = 1 \times 10^{-6}$ s.

Table 3   Farfield boundary condition

|			
velocity	v_∞	630	m s^{-1}
pressure	p_∞	1.0006×10^5	Pa
temperature	T_∞	113	K
Mach number	M_∞	2.907	

B. Pressure response

The pressure response amplitude spectrum for a simulation of the flat plate setup with an excitation frequency of $f_{FM} = 100$ Hz at three positions is shown in Fig. 12. The three positions along the moving plate shown in the figure correspond to nodes close to the joint (black, $x = 1$ mm) and two positions further downstream that are within the same range as the nozzle attached region's length (red, $x = 10$ mm and blue $x = 50$ mm). Similar to the pressure amplitude spectrum obtained from the nozzle simulation and shown in Fig. 7, the amplitude of the excitation frequency (marked with a dashed line) shows the highest value whereas the peaks for the whole number multiples are distinct but have much lower values that significantly decrease with increasing frequency. The reduced simulation setup seems to well reproduce the pressure response observed in the nozzle simulation.

For an inviscid fluid and a sufficiently low frequency the expected pressure wave's amplitude can be calculated analytically from the flow deflection by using the relations for a Prandtl-Meyer expansion fan and an oblique shock wave. With these assumptions, the flow conditions given in table 3, and a deflection of $\pm 1°$, an expected amplitude of the pressure wave of 7.57×10^3 Pa can be calculated. The best agreement with the made assumptions is expected for low excitation frequencies, i.e. quasi-stationary conditions, and positions sufficiently far downstream of the plate's joint and lambda shaped shock system. For an excitation frequency of $f_{FM} = 100$ Hz and an axial position of $x = 50$ mm the difference of the amplitude obtained by the Fourier transform and the analytical reference value is as low as 1.1 %.
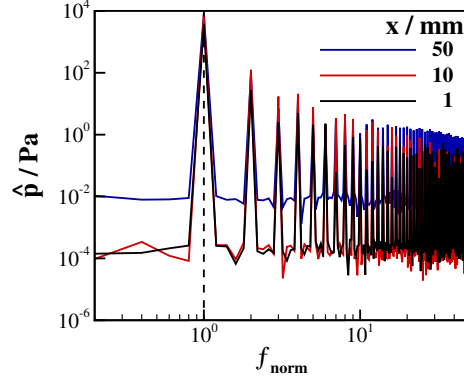
**Fig. 12 Pressure amplitude $\hat{p}$ spectrum for flat plate excited with $f_{FM} = 100\,\text{Hz}$**

To further support assumption *A2* of a downstream moving axial wave the phase shift $\Delta\Phi_P$ over the axial position x along the plate is shown in Fig. 13 for different excitation frequencies f_{FM}. For the lower frequencies the phase shift follows a linear distribution, as one would expect for a downstream moving pressure wave with constant velocity v_{pw}. The phase shift's gradient of the results with $f_{FM} = 2\,\text{kHz}$ decreases with increasing running length. This effect is caused by the limited pressure disturbance propagation velocity. For the highest frequencies investigated the wall's velocity becomes significantly large when compared to the speed of sound in the fluid. The pressure fluctuation leads to a compression of the fluid because it can not be emitted to the farfield fast enough. All large scale deformation effects observed in the unstable coupled nozzle simulation have characteristic frequencies much smaller than this value. The described effect is therefore of little significance for the further investigation.
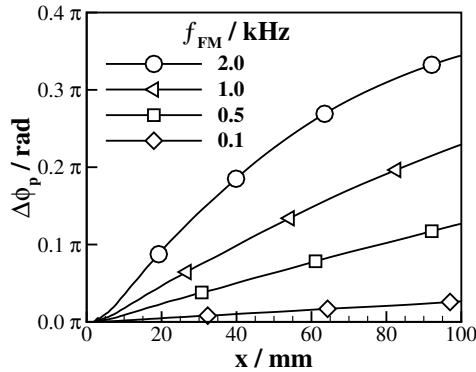
Fig. 13 Pressure phase shift $\Delta\Phi_P$ over axial position for flat plate

To obtain the wave propagation velocity from the phase shift distribution, function Eq. (33) has been fitted to the data shown in a range of $x_{fit} = [0, 10\,\text{mm}]$. With Eq. (34) the wave propagation velocity can then be calculated, which is shown in Fig. 14b for all excitation frequencies. For the flat plate with constant farfield boundary conditions the pressure disturbance velocity can be calculated from the convective velocity and the speed of sound. For the vicinity of the boundary layer ($z = 1\,\text{mm}$) this velocity has been calculated from the flow field for a snapshot of the simulation with

f_{FM} = 100 Hz at maximum displacement of the plate and is shown in Fig. 14a. The lambda shaped shock root at the plates joint causes a delayed drop of this velocity. Downstream the shock the propagation velocity is further decreased due to viscous effects and the aforementioned compression of the fluid by the moving plate. The wave propagation velocity obtained from the pressure response phase shift complies well with the expected downstream propagation speed.


a)   b)
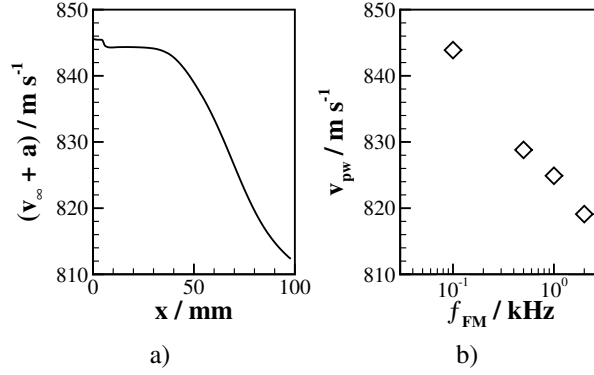
Fig. 14   Wave propagation velocity v_{pw} as obtained from a) the boundary layer vicinity b) the linear fit to pressure phase shift

The pressure response of the bent flat plate simulation setup shows good agreement with the explanation by the existence of a downstream moving axial pressure wave originated at the plates joint. Because the characteristics of the pressure response are similar to those observed in the nozzle simulation data and the setup and boundary conditions have been chosen to be as close to the original ones as possible, this also supports assumption *A2* made in Sec. V.D.

VII. Intrinsic oscillations

Using the same mesh and boundary conditions as in the forced motion setup, an unsteady CFD simulation without any deformation, or other external excitation, was performed to investigate self excited oscillations and support assumption *A3* made in Sec. V.D. A physical time step size of $\Delta t = 1 \times 10^{-5}$ s has been chosen. Further decreasing the time step showed no effect onto the results discussed in this section, but significantly increases the numerical effort needed to supply enough data to resolve the low frequency range by a fast Fourier transform. Figure 15 shows the spectrum of the pressure $\hat{p}_w$ at three axial positions in the attached region (blue, $X = 6$) and two in the recirculation region (red, $X = 9$ and black, $X = 10$). The shown data have been collected from nodes with an angular distance of 5° around the whole perimeter, because in the rotational symmetric geometry the flow patterns have no distinct orientation in circumferential position.

The pressure amplitude spectrum shown in Fig. 15 shows very low values over all frequencies for the attached region (blue) comparable to the plateau value between the peaks of the harmonics observed in the forced motion simulations shown in Fig. 7. In the recirculation region (black, red) the amplitude is significantly higher and also comparable to the aforementioned forced motion case. The spectrum shows a plateau up to a frequency of approximately
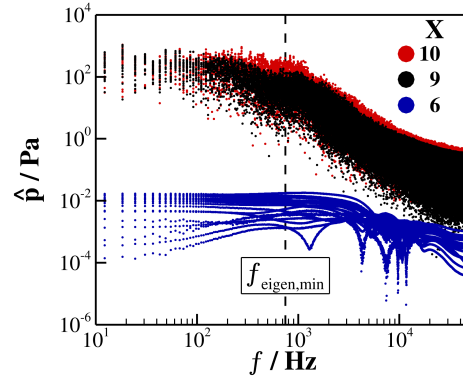
Fig. 15 **Pressure amplitude $\hat{p}$ spectrum for undeformed nozzle in attached (blue) and recirculation region (black, red)**

200 ($X = 9$, black) to 500 Hz ($X = 10$, red) and an exponential decrease for higher frequencies. This distribution complies well with experimental data for separated supersonic nozzles, the typical shape obtained from turbulent structure theory and semi-empirical models [62–64]. The turbulence generated over the separation shock causes the fluctuations that develop in the fluid downstream. In addition to the pressure amplitude obtained by a Fourier transform, the frequency of the lowest eigenfrequency of the unstable structure $f_{eigen,min}$ is marked in Fig. 15 by a dashed vertical line. The marked frequency is close to the transition from constant to lowering amplitude values, indicating that the lowest eigenfrequencies of the structure are affected the most by the fluctuations in the recirculation region. Although the described fluctuations are not harmonic and show no constant or clearly frequency dependent phase but are best characterized as noise, they still might excite a local initial deformation that propagates and increases over time when applied to flexible structures. The shown amplitude spectrum facilitates the excitation of the deformation modes with the lowest eigenfrequencies of the structure.

It should be noted that the used numerical model is not capable to resolve the highest frequencies shown in the pressure amplitude spectrum. Because of the spatial resolution and the applied turbulence model, fluctuations with small length scales and high frequencies are either resolved incorrectly or modeled within the equations. However, the resulting transient loads are nevertheless applied to the structures FEM model and contribute to the coupled systems overall stability. The effect of this unphysical numerical contribution is small when compared to that of the inclination- or the wave-superposition-effect due to the small amplitude.

For all frequencies and positions the amplitude spectrum of the undeformed nozzle complies well with that of the forced motion simulations. This supports assumption *A3* because no external excitation has caused these fluctuations in the simulation discussed in this section.

VIII. Conclusion

Forced motion simulations applying the eigenmodes of the subscale model of a rocket engine nozzle were carried out to understand the self-exciting mechanisms of fluid-structure interaction in an overexpanded subscale cold gas rocket engine nozzle. In the attached region, upstream the flow separation, the external excitation leads to a harmonic oscillation of the wall pressure. For low excitation frequencies the phase shift of the pressure response indicates that this region damps the transient deformation. The distribution of this phase shift is of particular interest because it is close to a value of π which indicates the transition from a damping to an exciting mechanism and shows a frequency-dependent gradient in axial direction. It could be shown that, additional to the expected standing wave created by the inclination change of the wall, a pressure wave is created at the flexible structure's interface and moves downstream along the nozzle wall. Additional simulations using a simplified bent flat plate simulation setup support this explanation and verify that the wave propagation velocity complies with the information propagation velocity in the fluid. Downstream the flow separation and the shock system the transient pressure response is mostly independent of the external excitation mechanism. The observed intrinsic oscillation in this recirculation region can be best characterized as a broadband noise caused by the turbulence created by the shock system. Although the transient part of the pressure response in this region does not affect an external excitation directly, it is strongest in the range of the lowest structure eigenfrequencies and can act as initial deformation mechanism for fluid structure interaction.

All of the described mechanisms have the strongest effect for low frequencies. Overall this facilitates the development and dynamic excitation of a displacement in the shape of the nozzle's eigenmode with the lowest eigenfrequency as observed in a preceding numerical investigation.

Funding Sources

References

[1] Cikanek, H. A., "Characteristics of Space Shuttle Main Engine Failures," *23rd Joint Propulsion Conference*, AIAA Paper 1987-1939, San Diego, USA, 1987. https://doi.org/10.2514/6.1987-1939.

[2] Watanabe, Y., Sakazume, N., and Tsuboi, M., "LE-7A Engine Nozzle Problems during Transient Operations," *38th AIAA/ASME/SAE/ASEE Joint Propulsion Conference & Exhibit*, AIAA Paper 2002-3841, Indianapolis, USA, 2002. https://doi.org/10.2514/6.2002-3841.

[3] Shi, J. J., "Rocket Engine Nozzle Side Load Transient Analysis Methodology- a Practical Approach," *46th*

AIAA/ASME/ASCE/AHS/ASC Structures, Structural Dynamics and Materials Conference, AIAA Paper 2005-1860, Austin, USA, 2005. https://doi.org/10.2514/6.2005-1860.

[4] Summerfield, M., Foster, C. R., and Swan, W. C., "Flow Separation in Overexpanded Supersonic Exhaust Nozzles," *Jet Propulsion*, Vol. 24, No. 5, 1954, pp. 319–321. https://doi.org/10.2514/8.6538.

[5] Tuovila, W. J., and Land, N. S., "Experimental Study of Aeroelastic Instability of Overexpanded Rocket Nozzle Extensions," NASA Technical Note NASA-TN-D-4471, NASA Langley Research Center, Hampton, USA, Apr. 1968.

[6] Nave, L. H., and Coffey, G. A., "Sea Level Side Loads in High-Area-Ratio Rocket Engines," *9th Propulsion Conference*, AIAA Paper 1973-1284, Las Vegas, USA, 1973. https://doi.org/10.2514/6.1973-1284.

[7] Holland, W., "SSME/Side Loads Analysis for Flight Configuration," NASA Technical Memorandum NASA-TM-X-64841, NASA Marshall Space Flight Center, Alabama, USA, Sep. 1974.

[8] Pekkari, L.-O., "Aeroelastic Stability of Supersonic Nozzles with Separated Flow," *29th Joint Propulsion Conference and Exhibit*, AIAA Paper 1993-2588, Monterey, USA, 1993. https://doi.org/10.2514/6.1993-2588.

[9] Frey, M., "Behandlung von Strömungsproblemen in Raketendüsen bei Überexpansion," Ph.D. thesis, Universität Stuttgart, Stuttgart, Germany, 2001. https://doi.org/10.18419/opus-3650.

[10] Östlund, J., "Flow Processes in Rocket Engine Nozzles with Focus on Flow Separation and Side-Loads," Ph.D. thesis, KTH Royal Institute of Technology, Stockholm, Sweden, 2002.

[11] Lefrançois, E., Dhatt, G., and Vandromme, D., "Fluid-Structural Interaction with Application to Rocket Engines," *International Journal for Numerical Methods in Fluids*, Vol. 30, No. 7, 1999, pp. 865–895. https://doi.org/10.1002/(SICI)1097-0363(19990815) 30:7<865::AID-FLD870>3.0.CO;2-5.

[12] Lefrançois, E., Dhatt, G., and Vandromme, D., "Numerical Study of the Aeroelastic Stability of an Overexpanded Rocket Nozzle," *Revue Européenne des Éléments Finis*, Vol. 9, No. 6-7, 2000, pp. 727–762. https://doi.org/10.1080/12506559.2000.10511483.

[13] Chen, C. L., Chakravarthy, S. R., and Hung, C. M., "Numerical Investigation of Separated Nozzle Flows," *AIAA Journal*, Vol. 32, No. 9, 1994, pp. 1836–1843. https://doi.org/10.2514/3.12181.

[14] Nasuti, F., and Onofri, M., "Viscous and Inviscid Vortex Generation During Startup of Rocket Nozzles," *AIAA Journal*, Vol. 36, No. 5, 1998, pp. 809–815. https://doi.org/10.2514/2.440.

[15] Deck, S., and Guillen, P., "Numerical Simulation of Side Loads in an Ideal Truncated Nozzle," *Journal of Propulsion and Power*, Vol. 18, No. 2, 2002, pp. 261–269. https://doi.org/10.2514/2.5965.

[16] Gross, A., and Weiland, C., "Numerical Simulation of Separated Cold Gas Nozzle Flows," *Journal of Propulsion and Power*, Vol. 20, No. 3, 2004, pp. 509–519. https://doi.org/10.2514/1.2714.

[17] Shimizu, T., Miyajima, H., and Kodera, M., "Numerical Study of Restricted Shock Separation in a Compressed Truncated Perfect Nozzle," *AIAA Journal*, Vol. 44, No. 3, 2006, pp. 576–584. https://doi.org/10.2514/1.14288.

[18] Ruf, J., McDaniels, D., and Brown, A., "Nozzle Side Load Testing and Analysis at MSFC," *45th AIAA/ASME/SAE/ASEE Joint Propulsion Conference & Exhibit*, AIAA Paper 2009-4856, Denver, USA, 2009. https://doi.org/10.2514/6.2009-4856.

[19] Schwane, R., and Xia, Y., "Time-Accurate CFD Predictions and Data Validation for Side Load Generation by Flow-Structure Coupling in Over-Expanded Rocket Nozzles," *Journal of Mathematical Modelling and Algorithms*, Vol. 4, No. 1, 2005, pp. 53–65. https://doi.org/10.1007/s10852-004-3522-2.

[20] Wang, T.-S., Lin, J., Ruf, J., and Guidos, M., "Transient Three-Dimensional Side-Load Analysis of Out-of-Round Film-Cooled Nozzles," *Journal of Propulsion and Power*, Vol. 27, No. 4, 2011, pp. 899–907. https://doi.org/10.2514/1.B34082.

[21] Wang, T.-S., Lin, J., and Guidos, M., "Transient Side-Load Analysis of Out-of-Round Film-Cooled Nozzle Extensions," *Journal of Propulsion and Power*, Vol. 29, No. 4, 2013, pp. 855–866. https://doi.org/10.2514/1.B34812.

[22] Winterfeldt, L.-O., Laumert, B., Tano, R., James, P., Geneau, F., Blasi, R., and Hagemann, G., "Redesign of the Vulcain 2 Nozzle Extension," *41st AIAA/ASME/SAE/ASEE Joint Propulsion Conference & Exhibit*, AIAA Paper 2005-4536, Tucson, USA, 2005. https://doi.org/10.2514/6.2005-4536.

[23] Brown, A. M., Ruf, J., Reed, D., D'Agostino, M., and Keanini, R., "Characterization of Side Load Phenomena Using Measurement of Fluid/Structure Interaction," *38th AIAA/ASME/SAE/ASEE Joint Propulsion Conference & Exhibit*, AIAA Paper 2002-3999, Indianapolis, USA, 2002. https://doi.org/10.2514/6.2002-3999.

[24] Moreaux, N., and Girard, S., "Experimental Assessment of Aeroelastic Coupling in a Rocket Engine Nozzle," *International Forum on Aeroelasticity and Structural Dynamics*, Amsterdam, Netherlands, 2003.

[25] Gradl, P. R., and Valentine, P. G., "Carbon-Carbon Nozzle Extension Development in Support of In-space and Upper-Stage Liquid Rocket Engines," *53rd AIAA/SAE/ASEE Joint Propulsion Conference*, AIAA Paper 2017-5064, Atlanta, USA, 2017. https://doi.org/10.2514/6.2017-5064.

[26] Eitner, M. A., Miller, B. G., Sirohi, J., and Tinney, C. E., "Operational Modal Analysis of a Thin-Walled Rocket Nozzle Using Phase-Based Image Processing and Complexity Pursuit," *37th IMAC, A Conference and Exposition on Structural Dynamics*, Springer International Publishing, Orlando, USA, 2019. https://doi.org/10.1007/978-3-030-12935-4_3.

[27] Lüdeke, H., Bartolome Calvo, J., and Filimon, A., "Fluid Structure Interaction at the Ariane-5 Nozzle Section by Advanced Turbulence Models," *European Conference on Computational Fluid Dynamics*, TU Delft, ECCOMAS, Egmond aan Zee, Netherlands, 2006.

[28] Blades, E. L., Baker, M., Pray, C. L., and Luke, E. A., "Fluid-Structure Interaction Simulations of Rocket Engine Side Loads," *SIMULIA Customer Conference*, Dassault Systemes, Providence, USA, 2012. https://doi.org/10.2514/6.2012-3969.

[29] Zhao, X., Bayyuk, S., and Zhang, S., "Aeroelastic Response of Rocket Nozzles to Asymmetric Thrust Loading," *Computers & Fluids*, Vol. 76, 2013, pp. 128–148. https://doi.org/10.1016/j.compfluid.2013.01.022.

[30] Wang, T.-S., Zhao, X., Zhang, S., and Chen, Y.-S., "Development of an Aeroelastic Modeling Capability for Transient Nozzle Flow Analysis," *Journal of Propulsion and Power*, Vol. 30, No. 6, 2014, pp. 1692–1700. https://doi.org/10.2514/1.B35277.

[31] Zhang, J. A., Shotorban, B., and Zhang, S., "Numerical Experiment of Aeroelastic Stability for a Rocket Nozzle," *Journal of Aerospace Engineering*, Vol. 30, No. 5, 2017, pp. 746–756. https://doi.org/10.1061/(ASCE)AS.1943-5525.0000746.

[32] Martelli, E., Ciottoli, P. P., Bernardini, M., Nasuti, F., and Valorani, M., "Detached-Eddy Simulation of Shock Unsteadiness in an Overexpanded Planar Nozzle," *AIAA Journal*, Vol. 55, No. 6, 2017, pp. 2016–2028. https://doi.org/10.2514/1.J055273.

[33] Reynaud, J., Weiss, P.-E., and Deck, S., "Numerical Workflow for Scale-Resolving Computations of Space Launcher Afterbody Flows with and without Jets," *Computers & Fluids*, Vol. 226, No. 104994, 2021. https://doi.org/10.1016/j.compfluid.2021.104994.

[34] Jack, S., and Génin, C., "Numerical and Experimental Investigation of Flow Separation in Ovalized Nozzles," *Space Propulsion Conference*, Köln, Germany, 2014.

[35] Jack, S., and Génin, C., "Flow Separation Study in Stiff Ovalized Rocket Nozzles, Part II: Numerical Approach," *51st AIAA/SAE/ASEE Joint Propulsion Conference*, AIAA Paper 2015-4154, Orlando, USA, 2015. https://doi.org/10.2514/6.2015-4154.

[36] Jack, S., and Oschwald, M., "Simulation of Fluid Structure Interaction in Overexpanded Cold Gas Rocket Nozzles Using the DLR TAU Code," *7th European Conference for Aeronautics and Space Sciences (EUCASS)*, Milano, Italy, 2017. https://doi.org/10.13009/EUCASS2017-206.

[37] Schwamborn, D., Gerhold, T., and Hannemann, V., "On the Validation of the DLR-TAU Code," *New Results in Numerical and Experimental Fluid Mechanics II*, Vol. 72, edited by E. H. Hirschel, K. Fujii, W. Haase, B. Van Leer, M. A. Leschziner, M. Pandolfi, A. Rizzi, B. Roux, W. Nitsche, H.-J. Heinemann, and R. Hilbig, Vieweg+Teubner Verlag, Wiesbaden, Germany, 1999, pp. 426–433. https://doi.org/10.1007/978-3-663-10901-3_55.

[38] Mack, A., and Hannemann, V., "Validation of the Unstructured DLR-TAU-Code for Hypersonic Flows," *32nd AIAA Fluid Dynamics Conference and Exhibit*, AIAA Paper 2002-3111, St. Louis, USA, 2002. https://doi.org/10.2514/6.2002-3111.

[39] Schwamborn, D., Gerhold, T., and Heinrich, R., "The DLR TAU-Code: Recent Applications in Research and Industry," *European Conference on Computational Fluid Dynamics*, TU Delft, ECCOMAS, Egmond aan Zee, Netherlands, 2006.

[40] Génin, C., and Jack, S., "Flow Separation Study in Stiff Ovalized Rocket Nozzles, Part I: Experimental Approach," *51st AIAA/SAE/ASEE Joint Propulsion Conference*, AIAA Paper 2015-4153, Orlando, USA, 2015. https://doi.org/10.2514/6.2015-4153.

[41] Rotta, J., "Statistische Theorie Nichthomogener Turbulenz," *Zeitschrift für Physik*, Vol. 129, No. 6, 1951, pp. 547–572. https://doi.org/10.1007/BF01330059.

[42] Launder, B., Reece, G., and Rodi, W., "Progress in the Development of a Reynolds-Stress Turbulence Closure," *Journal of Fluid Mechanics*, Vol. 68, No. 3, 1975, pp. 537–566. https://doi.org/10.1017/S0022112075001814.

[43] Daly, B. J., and Harlow, F. H., "Transport Equations in Turbulence," *Physics of Fluids*, Vol. 13, No. 11, 1970, pp. 2634–2649. https://doi.org/10.1063/1.1692845.

[44] Chou, P. Y., "On Velocity Correlations and the Solutions of the Equations of Turbulent Fluctuation," *Quarterly of Applied Mathematics*, Vol. 3, No. 1, 1945, pp. 38–54. https://doi.org/10.1090/qam/11999.

[45] Menter, F. R., "Two-Equation Eddy-Viscosity Turbulence Models for Engineering Applications," *AIAA Journal*, Vol. 32, No. 8, 1994, pp. 1598–1605. https://doi.org/10.2514/3.12149.

[46] Karl, S., Hickey, J.-P., and Lacombe, F., "Reynolds Stress Models for Shock-Turbulence Interaction," *31st International Symposium on Shock Waves*, Nagoya, Japan, 2019. https://doi.org/10.1007/978-3-319-91020-8_60.

[47] Jameson, A., "Transonic Flow Calculations," MAE Report 1651, Princeton University, Princeton, USA, Jul. 1983.

[48] Newmark, N. M., "A Method of Computation for Structural Dynamics," *Journal of the Engineering Mechanics Division*, Vol. 85, No. 3, 1959, pp. 67–94. https://doi.org/10.1061/TACEAT.0008448.

[49] Chung, J., and Hulbert, G. M., "A Time Integration Algorithm for Structural Dynamics With Improved Numerical Dissipation: The Generalized-α Method," *Journal of Applied Mechanics*, Vol. 60, No. 2, 1993, pp. 371–375. https://doi.org/10.1115/1.2900803.

[50] Spiering, F., Heinrich, R., and Keye, S., "Development of a Parallel Fluid-Structure Coupling Environment and Application to a Wind Tunnel Model under High Aerodynamic Loads," *New Results in Numerical and Experimental Fluid Mechanics VIII*, Vol. 121, edited by A. Dillmann, G. Heller, H.-P. Kreplin, W. Nitsche, and I. Peltzer, Springer Berlin Heidelberg, Berlin, Germany, 2013, pp. 507–514. https://doi.org/10.1007/978-3-642-35680-3_60.

[51] MacNeal, R. H., "A Simple Quadrilateral Shell Element," *Computers & Structures*, Vol. 8, No. 2, 1978, pp. 175–183. https://doi.org/10.1016/0045-7949(78)90020-2.

[52] Swiss Composite, "GFK Werkstoffdaten," , 2015. URL https://www.swiss-composite.ch/pdf/i-Werkstoffdaten.pdf?, [retrieved 8 February 2022].

[53] Roache, P. J., "Quantification of Uncertainty in Computational Fluid Dynamics," *Annual Review of Fluid Mechanics*, Vol. 29, No. 1, 1997, pp. 123–160. https://doi.org/10.1146/annurev.fluid.29.1.123.

[54] Rakowitz, M., "Grid Refinement Study with a UHCA Wing-Body Configuration Using Richardson Extrapolation and Grid Convergence Index GCI," *New Results in Numerical and Experimental Fluid Mechanics III*, Vol. 77, edited by

S. Wagner, U. Rist, H.-J. Heinemann, and R. Hilbig, Springer Berlin Heidelberg, Berlin, Germany, 2002, pp. 297–303. https://doi.org/10.1007/978-3-540-45466-3_36.

[55] Dowell, E. H., "Panel Flutter - A Review of the Aeroelastic Stability of Plates and Shells," *AIAA Journal*, Vol. 8, No. 3, 1970, pp. 385–399. https://doi.org/10.2514/3.5680.

[56] Muhlstein Jr., L., "A Forced-Vibration Technique for Investigation of Panel Flutter," *2nd Aerodynamic Testing Conference*, AIAA Paper 1966-769, Los Angeles, USA, 1966. https://doi.org/10.2514/6.1966-769.

[57] Lübker, J., and Alder, M., "Experimental Investigations on Aerodynamic Response of Panel Structures at High Subsonic and Low Supersonic Mach Numbers," *Transportation Research Procedia*, Vol. 29, 2018, pp. 222–232. https://doi.org/10.1016/j.trpro.2018.02.020.

[58] Alder, M., "Einfluss turbulenter Grenzschichten auf die aeroelastische Stabilität dünnwandiger Schalen," Ph.D. thesis, Technische Universität Braunschweig, Braunschweig, Germany, Jun. 2020.

[59] Stark, R., "Beitrag zum Verständnis der Strömungsablösung in Raketendüsen," Ph.D. thesis, Rheinisch Westfälisch Technische Hochschule Aachen, Aachen, Germany, Dec. 2010.

[60] Dowell, E. H., *A Modern Course in Aeroelasticity: Fifth Revised and Enlarged Edition*, Solid Mechanics and Its Applications, Vol. 217, Springer International Publishing, Cham, Germany, 2015. https://doi.org/10.1007/978-3-319-09453-3.

[61] Génin, C., Stark, R., and Jack, S., "Flow Separation in Out-of-Round Nozzles, a Numerical and Experimental Study," *Progress in Flight Physics*, Vol. 7, 2015, pp. 269–282. https://doi.org/10.1051/eucass/201507269.

[62] Dussauge, J.-P., Dupont, P., and Debiève, J.-F., "Unsteadiness in Shock Wave Boundary Layer Interactions with Separation," *Aerospace Science and Technology*, Vol. 10, No. 2, 2006, pp. 85–91. https://doi.org/10.1016/j.ast.2005.09.006.

[63] Johnson, A. D., and Papamoschou, D., "Instability of Shock-Induced Nozzle Flow Separation," *Physics of Fluids*, Vol. 22, No. 1, 2010, p. 016102. https://doi.org/10.1063/1.3278523.

[64] Hwang, Y., Bonness, W. K., and Hambric, S. A., "Comparison of Semi-Empirical Models for Turbulent Boundary Layer Wall Pressure Spectra," *Journal of Sound and Vibration*, Vol. 319, No. 1-2, 2009, pp. 199–217. https://doi.org/10.1016/j.jsv.2008.06.002.